HYDROCOASTAL

SAR/SARin Radar Altimetry for Coastal Zone and Inland Water Level

A hydraulic model of the Amur River informed with ICESat-2 elevation

Sentinel-3 and Cryosat SAR/SARin Radar Altimetry for Coastal Zone and Inland Water

ESA Contract 4000129872/20/I-DT

Project reference: HYDROCOASTAL_ESA_TN_WP3310
Issue: 1.0

This page has been intentionally left blank

Change Record

Date	Issue	Section	Page	Comment

Control Document

Process	Name	Date
Written by:	Peter Bauer-Gottwein	
Checked by		
Approved by:		

Subject	Radar Altimetry for Coastal Zone and Inland Water Level	Project	HYDROCOASTAL

Author	Organisation	Internal references
Peter Bauer-Gottwein	DTU	

	Signature	Date
For HYDROCOASTAL team		
For ESA		

Table of Contents

Contents

1. Summary

Accurate predictions of water surface elevation (WSE) in rivers at high spatial and temporal resolution are important for flood/drought risk assessment and flood/drought forecasting and management. WSE in a river is controlled by three main factors: discharge, riverbed geometry, and hydraulic roughness. In remote and poorly instrumented rivers, both discharge and riverbed geometry are highly uncertain and WSE is therefore hard to predict. ICESat-2 laser altimetry provides accurate elevation transects across the river at very high spatial resolution (70 cm along track). This study demonstrates how ICESat-2 elevation transects can be used to parameterize a basin-scale hydraulic model of a continental-scale river. The workflow is demonstrated for the transboundary Amur River in North-East Asia. Simulated WSE is subsequently validated against a large dataset of in-situ and satellite altimetry observations from the Hydrocoastal project, and we demonstrate that the model can reproduce available WSE observations throughout the basin with an accuracy of 1-2 meters. An earlier version of this report has been published as a preprint here https://doi.org/10.21203/rs.3.rs-2203742/v1 and is currently under review for publication.

2. Introduction

Rivers are highly vulnerable to climate extremes and, at the same time, essential for biodiversity and economic development. As a consequence of the 2022 drought and heat wave, which simultaneously affected all 3 major world economies (EU, US and China), the economic importance of rivers as transport waterways and cooling water reservoirs has come into increased focus. Improved quantitative tools for river management are thus important and timely.

State-of-the-art global scale inland water modeling and forecasting systems (e.g. GLOFAS, (Alfieri et al., 2013), EFAS, (Alfieri et al., 2014), DHI GHM, (Murray et al., 2023), World Wide HYPE, (Arheimer et al., 2020)) rely on the combination of numerical weather prediction systems and simulation models with observational datasets from in-situ sensors and satellite earth observation (EO). The hydrologic compartment of such systems typically includes two sub-models, one representing the rainfall-runoff phase of the inland water cycle, and second, a hydraulic model representing flow and inundation processes in rivers and floodplains. The hydraulic model is essential to transform runoff predictions provided by the rainfall-runoff model into predictions of water level along the river. Water level, in turn, is the controlling variable for flood risk assessment and flood early warning (Winsemius et al., 2013).

Parameterizing hydraulic models at continental to global scale remains challenging (Bjerklie et al., 2018; Neal et al., 2012; Pujol et al., 2020). A number of approaches have been developed, many of which exploit the increased availability of water surface elevation (WSE) observations from multiple satellite altimetry missions from databases such as Hydroweb (Crétaux et al., 2011) and Dahiti, (Schwatke et al., 2015) and use these datasets to fit simple conceptual river cross section shapes (e.g. Garambois et al., 2017; Jiang et al., 2019; Neal et al., 2012; Schneider et al., 2017). Problems that commonly arise in such workflows include parameter trade-offs between cross-sectional shape parameters and hydraulic roughness, as well as rapid changes in flow width occurring around the bankfull depth of the river, which cannot be captured with simple conceptual shapes. To resolve the inherent non-uniqueness of the hydraulic inverse problem, additional hydraulic observations from satellite EO, such as surface water extent and water surface slope have been used (Bjerklie et al., 2018; Pujol et al., 2020).

The ICESat-2 mission (Markus et al., 2017) provides new opportunities for the parameterization of large-scale hydraulic river models, because it delivers very high-resolution elevation datasets with an along-track resolution of just 70 cm (Neumann et al., 2019). ICESat-2 elevation transects across the river, taken during the low flow season, thus map the river cross section at a very high level of detail, with the exception of the submerged portion. While ICESat-2 can directly map submerged bathymetry in clear coastal waters (Parrish et al., 2019), in most cases, the submerged portion of the riverbed cannot be mapped from ICESat-2 data, because river water transparency is low and the laser beams do not penetrate through the water down to the river bed. However, during low-flow periods, the submerged portion of the riverbed is small. Rather than fitting the entire river cross section using conceptual shapes, one only has to extrapolate a small portion of the cross section that is submerged at ICESat-2 acquisition time. This reduces parameter trade-offs between cross section shape and friction parameters.
This report demonstrates how ICESat-2 elevation datasets can be used for the development of continental-scale hydraulic models and illustrates the workflows for the example of the Amur River. We show that a hydraulic model parameterized using ICESat-2 elevation transects across the river can reproduce water level observations from in-situ stations and the available inland water satellite altimetry record, consisting of more than one hundred virtual station time series placed along the river course. The workflows developed here are applicable at global scale and provide a consistent methodology for the simulation of water surface elevation in global rivers that can be combined with the global inland water record available from satellite altimetry.

3. Materials and Methods

3.1. The Amur River

The Amur (or Heilong Jiang in Chinese) is the world's 10th longest river with a total drainage basin of ca. 1.89 million km^2 and a total length of ca. 4440 km. The vast majority of the basin is located in Russia (53%) and China (45%). Mongolia hosts the remaining 2% of the basin area (Figure 3.1). Over a total distance of ca. 2500 km, the Amur River forms the border between China and Russia, and on this entire stretch of the river, no in-situ discharge observations are available. The Amur River ultimately drains into the Tatar Strait between the Sea of Okhotsk and the Sea of Japan. River width varies from a few hundred meters in the upstream reaches to several kilometers in the downstream portions of the river. The Amur River is a global biodiversity hotspot hosting endemic fish species and large migratory fish populations as well as huge wetland systems (Egidarev et al., 2016; Simonov et al., 2019). While floodplains on the Chinese side of the river have been severely affected by river regulation (Jia et al., 2020), wetlands in the Russian portions of the basin remain largely intact.
Because it is located in a latitude range from 41 to 56 degrees north, the basin is dominated by cold continental weather with dominant snowfall in winter. Large portions of the river are ice-covered during the winter months. Ice cover monitoring using satellite imagery and satellite altimetry datasets (Zakharova et al., 2021) confirms that the river is frozen from end-November to end-April. The Amur River has several large tributaries (Figure 3.1), the largest of which is the Songhua River, joining the Amur from the right-hand side near the town of Tongjiang in China. There are 19 large dams in the Amur River Basin (Simonov et al., 2019). Seven reservoirs have a storage capacity larger than 1 km^3, of which two are located in Russia and five in China (Figure 3.1). Flooding is common in the Amur basin and seasonal and inter-annual variations of river flow can be related to large-scale atmospheric patterns (Tachibana et al., 2008). The most recent disastrous flood occurred in 2013 (Danilov-Danilyan et al., 2014) and another

large flood occurred in 2019. The evolution of flood risk in a changing climate is of concern (Nohara et al., 2006; Yu et al., 2013).

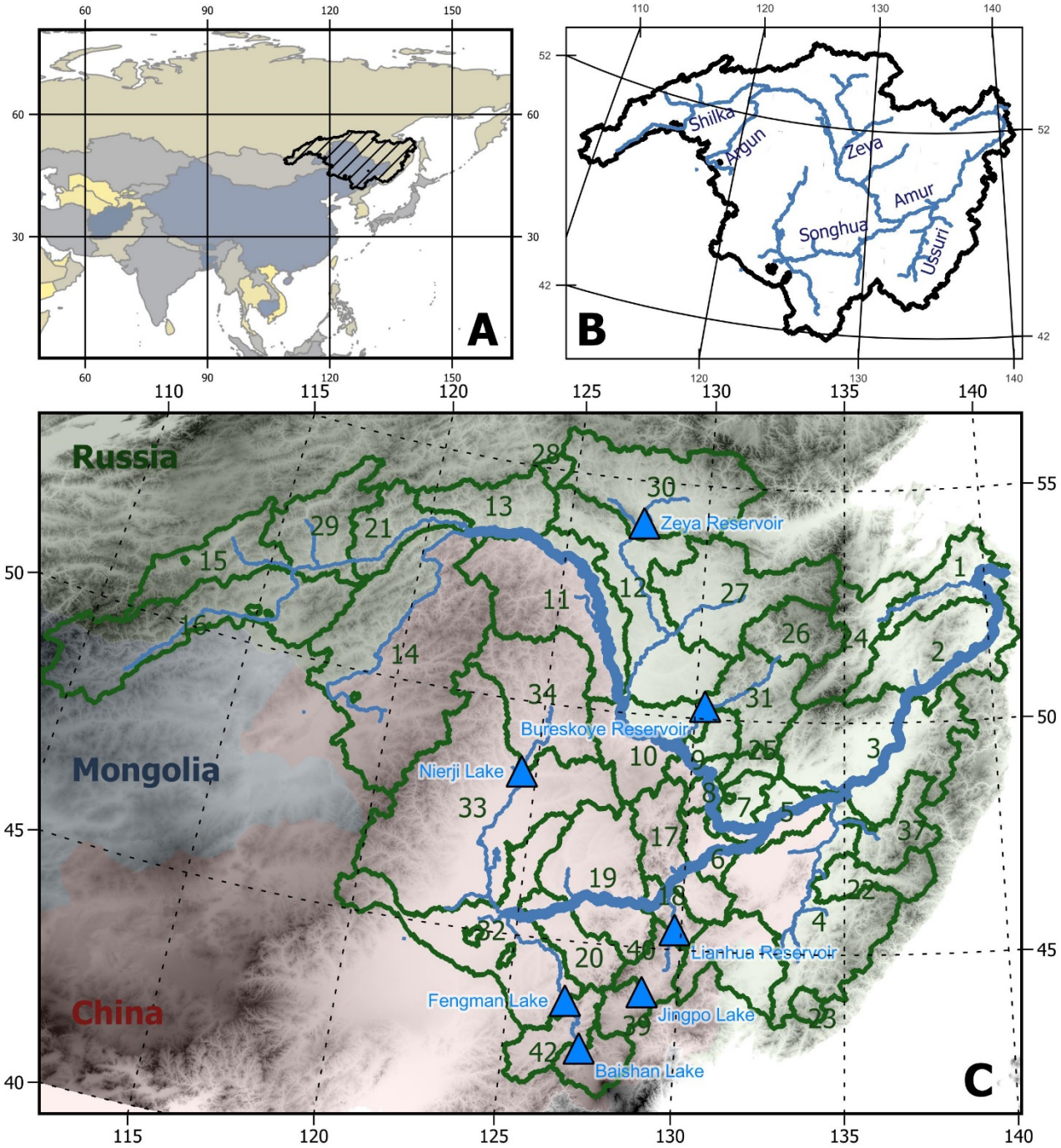

Figure 3.1 Base map of the Amur River system, indicating geographic location (A) and main rivers (B). Panel C shows reservoirs (blue triangles), routing branches of the model (thin blue lines), hydrodynamic branches (thick grey lines) and subcatchments of the model (green shapes). Background shading is SRTM elevation.

3.2. Rainfall-Runoff Modeling

In order to estimate spatio-temporally distributed runoff forcings for the hydraulic model of the Amur River, we set up and calibrate a basin-scale rainfall-runoff model, because available in-situ discharge records are sparse and unevenly distributed. Kalugin & Motovilov, 2018 report the only basin-scale rainfall-runoff modelling effort for the Amur in the open literature. We used the NAM rainfall runoff model (Nielson & Hansen, 1973), which is integrated into DHI's Mike Hydro River package, for rainfall-runoff simulation. The NAM rainfall-runoff model has been used and discussed in many hydrologic modelling studies reported in the international peer-reviewed literature (e.g. Andersen et al., 2006; Vansteenkiste et al., 2014; Zhu et al., 2008). The Amur River basin was divided into 43 individual subcatchments (Figure 3.1), using the MERIT hydro DEM (Yamazaki et al., 2019) and the hydrographic DEM processing software TauDEM (Tesfa et al., 2011). The rainfall-runoff model does not include the areas contributing to Lake Hulun in Mongolia, which is essentially endorheic and only occasionally overflows into the Argun River.

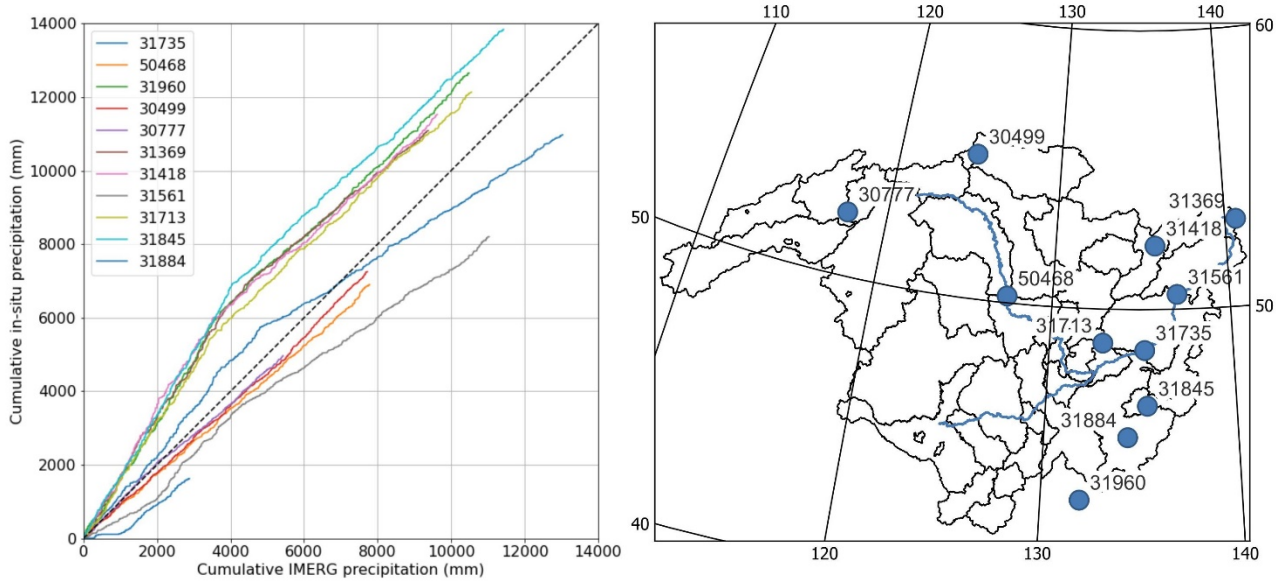

Figure 3.2 Double-mass plots for selected in-situ precipitation stations. The right panel shows the locations of the stations. The left panel plots cumulative station precipitation versus cumulative IMERG precipitation for the pixel on which the station falls. The in-situ observation period is 2008-2019 for all stations except 31884, for which it is 2016-2019.

As precipitation forcing for the NAM rainfall-runoff model, we used NASA's Global Precipitation Measurement (GPM) Integrated Multi-satellitE Retrievals for GPM (IMERG) product, more specifically the final precipitation L3 half hourly 0.1 degree x 0.1 degree product, version 06 (Huffman et al., 2019), aggregated to daily values. IMERG precipitation was evaluated against a few available in-situ precipitation stations, provided by the Russian Hydrometeorological Service, using straightforward grid-to-point comparison in the time period 2008-2019. Resulting double-mass plots are shown in Figure 3.2. The double-mass plots indicate inconsistencies and shifting biases between the stations and the IMERG product, which may be due to the IMERG product or due to issues with the in-situ instrumentation.

Table 3.1: Rainfall-runoff model calibration and validation results. RMSE is the root mean squared error, WBE the water balance error or bias, and NSE the Nash-Sutcliffe model efficiency.

Station	Catchment ID	IMERG Runoff coefficient	Calibration Period	Validation Period	RMSE (m^3/s) Calibration (% of mean flow)	RMSE (m^3/s) Validation (% of mean flow)	WBE (%) Cal.	WBE (%) Val.	NSE Cal.	NSE Val.	Calibration Climatology index	Validation Climatology index
Novomikhai-lovka	23	0.39	2008-2014	2015-2018	37.3 (74)	66.8 (133)	0.07	-3.70	0.57	0.49	0.17	0.42
Tynda	28	0.49	2008-2014	2015-2018	54.3 (127)	45.9 (107)	-1.00	2.71	0.54	0.55	0.30	0.34
Zvenievoy	22	0.45	2008-2014	2015-2018	159.6 (65)	183.1 (74)	-0.11	-3.70	0.65	0.68	0.31	0.49
Khor	37	0.71	2008-2014	2015-2018	341.8 (74)	351.3 (76)	22.30	20.70	0.54	0.48	-0.05	-0.07
Gouda	24	0.63	2008-2014	2015-2018	350.6 (61)	295.8 (52)	3.10	1.20	0.72	0.75	0.22	0.32
Ust-Niman	26	0.45	2008, 2010, 2011	2012, 2013	353.6 (109)	497.3 (153)	-2.20	17.50	0.42	0.42	-0.15	0.33
Birobidjan	25	0.63	2008-2014	2015-2018	98.1 (80)	97.5 (79)	11.20	7.70	0.60	0.45	0.21	0.06
Ust-Ulma	27	0.49	2008-2014	2015-2018	776.6 (100)	771.1 (99)	2.43	-7.00	0.52	0.48	0.01	0.17
Krasnoya-rovo	15	0.26	2008-2014	2015-2018	104.6 (85)	101.8 (83)	27.60	3.30	0.51	0.76	0.08	0.69
Dalai	33+34	0.12	2016-2018	2019	183.60 (40)	427.7 (93)	0.29	3.63	0.80	0.85	0.62	0.83
Mean									**0.59**	**0.59**	**0.17**	**0.36**

Because we do not have access to a spatially dense and quality-assured precipitation product based on in-situ monitoring networks in the region, and because the IMERG product has been shown to perform on par with in-situ precipitation when used as hydrological forcing in neighbouring regions of China (Jiang & Bauer-Gottwein, 2019), we force the rainfall-runoff model of the Amur river basin with the IMERG product. Gridded land surface (2m) temperature estimates were obtained from ERA5-Land hourly data, provided through the Copernicus Climate Data Store (Muñoz Sabater, 2019). Hourly temperature data were aggregated to daily maximum, minimum and average temperatures. Daily temperature statistics were used to estimate reference ET using the approach by (Hargreaves & Samani, 1985). In the NAM model, daily average temperature further controls snow accumulation and snow melt via a threshold temperature for snow fall and a temperature index parameterization of snowmelt (Hock, 2003).

For the 10 in-situ river discharge stations reported in Table 3.1, the NAM model was automatically calibrated assuming uniform parameters across the entire subcatchment corresponding to the station. Daily discharge data for the period 2008-2019 was obtained from the Russian Hydrometeorological Service for these stations. Daily discharge is obtained from daily water level observations using rating curves, which are seasonally variable and confirmed and updated with regular river gauging surveys. The accuracy of the discharge time series is not specified by the data provider, but is likely around 10%. In total, 9 NAM parameters (Umax, Lmax, CQOF, CKIF, CK1,2, TOF, TIF, TG and CKBF, please refer to Nielson & Hansen, 1973 and Madsen, 2000 for a description of NAM parameters) were automatically adjusted between reasonable a-priori bounds to minimize overall root mean square error between simulated and observed runoff and overall water balance error, using a global search algorithm as described in (Madsen, 2000). Performance was benchmarked against the mean of all observations using the Nash-Sutcliffe Efficiency (NSE). NSE produces optimistic skill scores for seasonal rivers and we therefore also report a skill score in which runoff climatology (i.e. the average of all historical runoff observations for a given day of the year) was used as the benchmark. The climatology index (CI) is calculated as (see also (Bennett et al., 2013))

$$\boldsymbol{CI = 1 - \frac{RMSE_{NAM}}{RMSE_{Clim}}} \qquad \textbf{Equation 1}$$

where $RMSE_{NAM}$ is the root mean squared error between the observations and the NAM simulation and $RMSE_{Clim}$ is the root mean squared error between the observations and the runoff climatology.

Transfer of NAM parameters to ungauged subcatchments was based on catchment similarity, using an approach described in Kittel et al., 2020. We used average rainfall, average temperature and average terrain slope as the attributes defining similarity. Ungauged catchments inherited parameters from the gauged catchment that was closest in terms of total normalized distance between the attributes of the two catchments. The standard deviations of the attributes across all 43 subcatchments were used to normalize the distances. Parameter transfer relationships between catchments are illustrated in Figure 3.3.

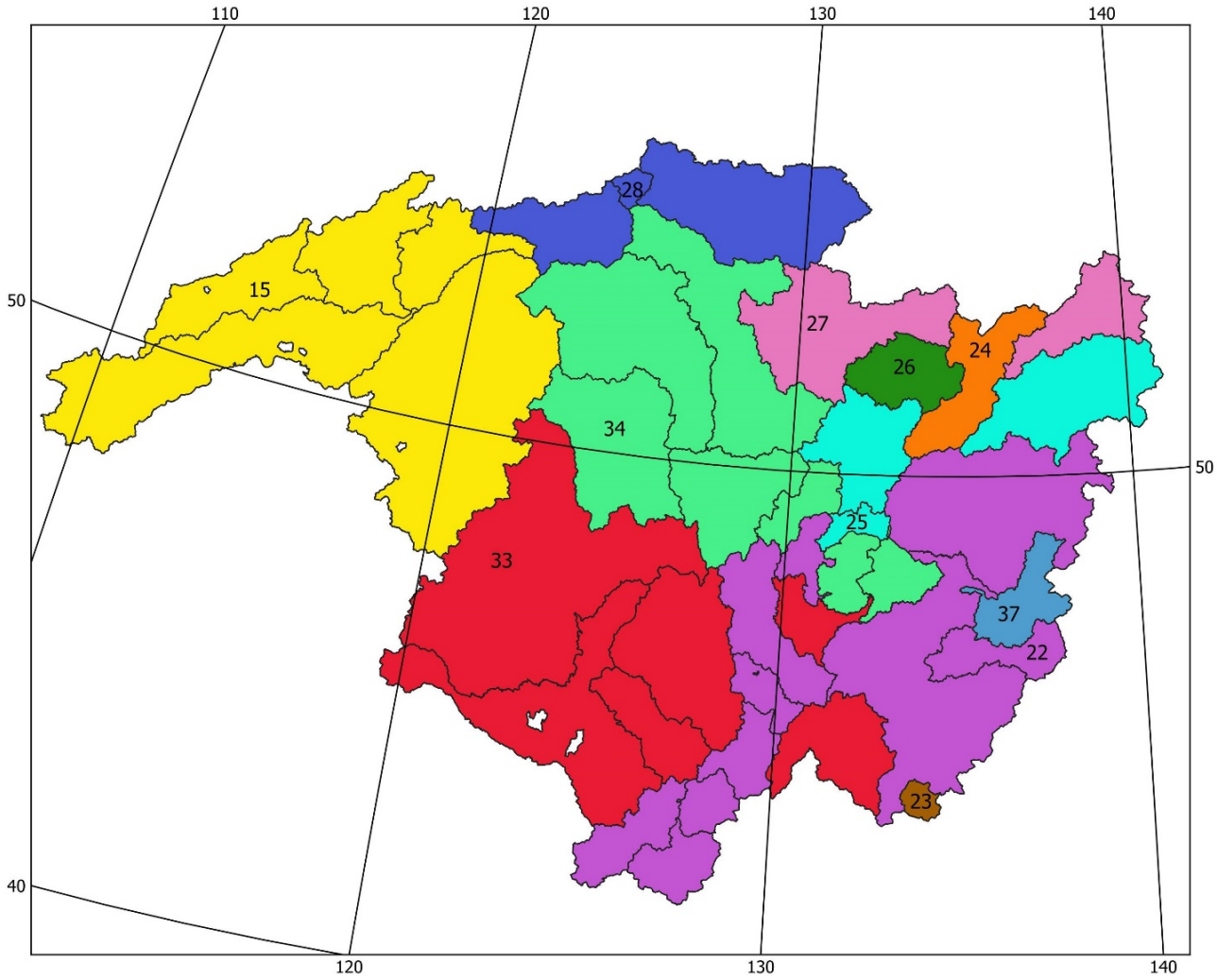

Figure 3.3: Parameter transfer from gauged to ungauged subcatchments. NAM parameters calibrated for the numbered catchments were transferred to all catchments with the same colour code.

3.3. Processing of ICESat-2 land elevation datasets

ICESat-2 is a spaceborne green lidar mission (532nm), mapping the Earth's surface at unprecedented spatial resolution of approx. 70 cm along track since 2018 (Markus et al., 2017). ICESat-2 is configured with 3 beam pairs that allow for across-track slope determination (90m between pair members and 3.3km between pairs). Each beam pair includes a strong beam (right with respect to orbit direction) and a weak beam (left with respect to orbit direction) with a power ratio of 4:1. ICESat-2 is on a 91-day repeat orbit, for this reason the ground sampling pattern is very dense, while the temporal resolution is low. We used two different ICESat-2 data products: ATL08, which is a low-resolution terrain elevation product (Neuenschwander & Pitts, 2019) and ATL03, which is the native-resolution geolocated photon product (Neumann et al., 2019). We used version 5 of both products and accessed the data through the online portal of the US National Snow and Ice Data Center (https://nsidc.org/data/atl08/versions/5).

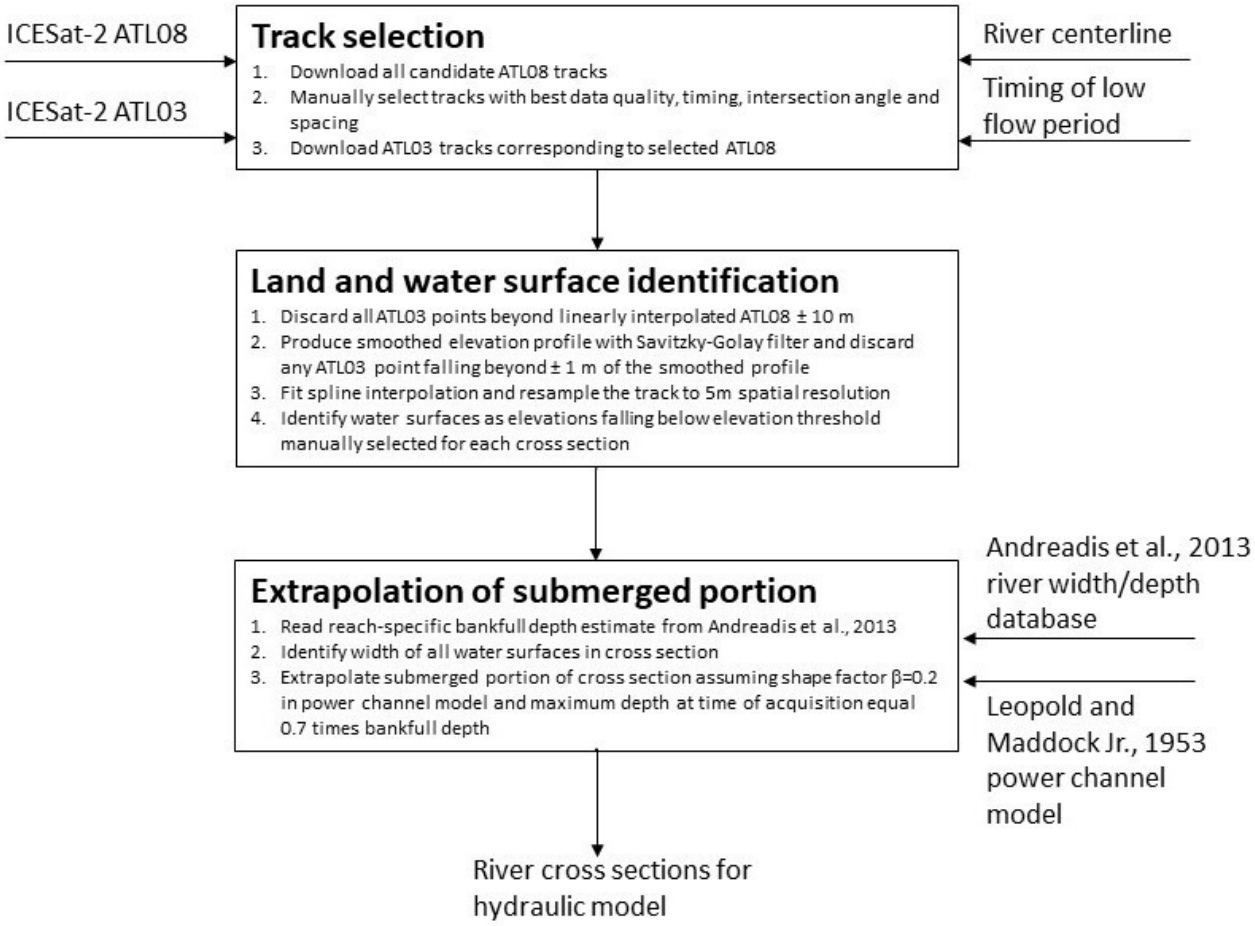

Figure 3.4: Flow chart for the delineation of river cross section geometry from ICESat-2 data products

The Amur riverbed geometry was extracted from ICESat-2 elevation transects across the Amur River following the workflow outlined in Figure 3.4. ATL08 ground tracks were manually inspected to find crossings, spaced approximately every 10-20 river-km, with sufficient data density over the area of interest, which were directed approximately perpendicularly to the river centerline. The ICESat-2 laser is sensitive to cloud cover and mist, which strongly reduces the number of crossings that can be used to extract cross-section geometry. Moreover, we only used crossings during the dry and frozen season (i.e. November to April), when water levels in the river are low and a large portion of the cross section geometry is therefore exposed and observable by ICESat-2. The selected ATL08 transects were used to pre-filter the corresponding ATL03 transects and ATL03 data points with elevations outside ±10m of the interpolated ATL08 elevation were rejected. Remaining ATL03 data was smoothed with a Savitzky-Golay filter (Savitzky & Golay, 1964) using a 3rd degree polynomial to fit the ATL03 points and a variable window length to achieve appropriate smoothing of the ATL03 point cloud. Variable window length was necessary, because cross sections had different absolute length, ranging from hundreds of meters in the upstream portions of the river to tens of kilometres in the large floodplains, and because ATL03 point density varied greatly with atmospheric conditions. All ATL03 points falling more than 1m from the

filtered line were removed. The surface elevation geometry was created with a smoothing spline function from the remaining ATL03 points. The degree of smoothing was controlled manually for each cross section to achieve an appropriate representation of the elevation profile. Using the spline interpolation, cross section geometry was resampled to 5m spatial resolution. Open water surfaces were identified in the cross section as entirely flat and smooth surfaces. In the ATL03 datasets for the Amur cross sections used here, we have been unable to detect useable returns from the submerged riverbed. In some sections, we see scattered photons returned from below the water surface, which may be reflected from the riverbed, but the signal-to-noise ratio is too low to enable robust retrieval of submerged riverbed geometry. For this reason, submerged riverbed elevation was extrapolated using the power channel model (Leopold & Maddock Jr., 1953). The power channel model can be written as

$$A = \alpha \cdot d^{\beta}$$
$$w = \frac{\partial A}{\partial d} = \alpha \cdot \beta \cdot d^{\beta-1} \qquad \textbf{Equation 2}$$

where A is the flow cross sectional area, w is the flow surface width, and d is the flow depth. The parameters α and β are empirical fitting parameters. We assumed a uniform value of the shape parameter β (=0.2). Depths were estimated as 0.7 times the bankfull depths reported in Andreadis et al., 2013 and available online at http://gaia.geosci.unc.edu/rivers/. In the downstream reaches of the Amur River, which are affected by backwater from the ocean, depths for ICESat-2 cross section acquisition dates were assumed to be equal to the bankfull depths reported in Andreadis et al., 2013. Parameters α were subsequently determined for each cross section from the assumed depth and β and the observed flow width from ICESat-2. Once the parameters of the power channel model were determined, we estimated the submerged riverbed elevation at 5m along-track spacing from the power channel model and prepared the final cross section for input into the hydraulic model. This included tagging each cross section with the corresponding river chainage, the angle of intersection with the river centerline and sorting the elevations in the direction from left bank to right bank. For selected cross sections, a priori estimates of depth were subsequently manually updated to match simulated spatio-temporally distributed water surface elevations to observed WSE data from in-situ stations and satellite radar altimetry, see section on model validation below.

3.4. Hydraulic modelling

Hydraulics in the main branches of the Amur and Songhua rivers (thick blue lines in Figure 3.1) were simulated using the fully dynamic version of the 1-dimensional De Saint-Venant equations. Tributary flow (i.e. thin blue reaches in Figure 3.1) was simulated using Muskingum routing (Chow, 1988), assuming a kinematic wave speed of 100 km per day and Muskingum's X=0.25. The estimates of the Muskingum routing parameters are reasonable but cannot be validated with the available field observations. Muskingum parameters were varied manually, but showed low sensitivity to the simulated water surface elevation in the main Amur and Songhua rivers. The 7 major reservoirs in the basin (Figure 3.1) were implemented as storage nodes in the Muskingum routing scheme. Evaporation from the open reservoir water surface was neglected and, in the absence of information on reservoir operation, the regulated outflow was determined using a standard operation policy (SOP, Maass et al., 1962) with the target release equal to the annual average runoff and the flood control volume equal to the reservoir storage capacity. This very approximate representation of reservoir regulation will cause significant errors in simulated river flow locally, but, because only a small fraction of total runoff is regulated, the impact on

simulated flows in the main Amur and Songhua River reaches is expected to be moderate. As an alternative, target volume regulation was implemented based on reservoir water storage changes observed with satellite EO. The results obtained from these runs showed that reservoir regulation only affects water levels in the low-flow period and differences in simulated water levels are generally less than a meter.
A numerical hydrodynamic model for the main Amur and Songhua River reaches was implemented in the Mike Hydro River software (Havnø et al., 1995), which uses a 6-point finite difference scheme on a staggered grid to solve the coupled continuity and momentum equations (Abbott & Ionescu, 1967). We used a maximum grid spacing of 5 km and a fixed time step of 5 minutes in the numerical solution. The hydrodynamic model was forced with boundary runoff from the rainfall-runoff model and the tributary routing reaches. At the ocean boundary, a constant water level at 0 mamsl was assumed. This will introduce significant model errors locally, because the coastal water level in the Tatar Strait, into which the Amur River flows, is subject to significant tidal variations. However, boundary errors only affect simulated water levels a few tens of km upstream of the boundary. Cross section geometry was imported from the ICESat-2 processing results described in section 3.3. We parameterized the friction between the flow and the riverbed using Manning's equation, which expresses the friction slope as dependent on the roughness parameter (Manning's n), the cross section geometry, and the water level (Chow, 1988). We assumed a global uniform value of Manning's n equal to 0.033 $s/m^{1/3}$ during the unfrozen period, except for the most downstream 200-km section of the Amur River, where n = 0.013 $s/m^{1/3}$ was assumed. Moreover, Manning's n during the frozen period of the river (end November to end April) was assumed to be 3 times as high as during the unfrozen period and a transition period of 15 days was assumed between frozen and unfrozen states, over which Manning's n was assumed to vary linearly in time. The factor of 3 between the Manning numbers for frozen and unfrozen states was derived from the inspection of in-situ rating curves prepared by the Russian Hydrometeorological Service, who use different rating curves in the frozen and unfrozen periods (Kouraev et al., 2004).

3.5. Validation with satellite-derived and in-situ water surface elevation datasets

In order to validate the hydraulic model and demonstrate its value for water level prediction, simulated water levels were compared with in-situ station datasets from 12 stations (7 in Russia and 5 in China, see Figure 3.5) and dozens of satellite altimetry virtual stations (VS, Figure 3.5). We included all satellite altimetry time series available on the Hydroweb database (Crétaux et al., 2011, https://hydroweb.theia-land.fr/), for the simulated domain, i.e. 116 virtual station time series in total. For all in-situ and virtual stations, water level time series were extracted from the hydrodynamic model results and were directly compared with the observations. Because we referenced the ICESat-2 cross sections to the EGM2008 geoid model (Pavlis et al., 2012), simulated water surface elevation was also referenced to EGM2008, as were all the satellite altimetry observations at VS. The vertical reference of the in-situ stations was unknown and we therefore expect time-constant bias between the model and the in-situ observations.
As an alternative, the Hydrocoastal L3 dataset for the Amur River was also used to validate the hydraulic model. The Hydrocoastal L3 dataset is comparable in terms of density of VS to the Hydroweb database, with 156 VS available on the rivers included in the hydraulic model (compared to 116 from Hydroweb).

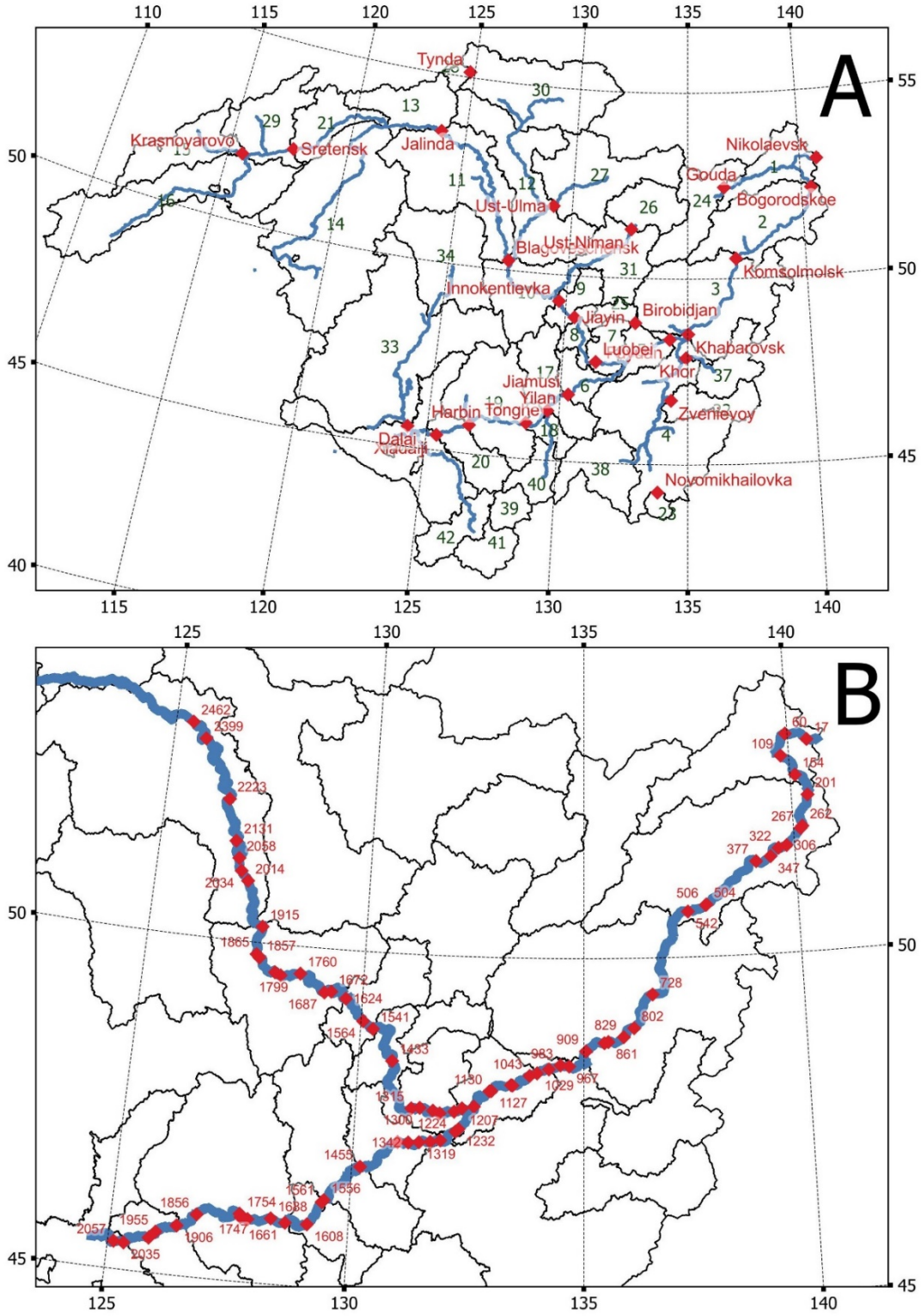

Figure 3.5: Overview of in-situ and virtual stations in the Amur River Basin. Panel A: In-situ stations; Panel B: Hydroweb virtual stations labelled with the river-kilometers used in the Hydroweb database (https://hydroweb.theia-land.fr/)

4. Results and Discussion

4.1. Hydrologic model calibration and validation results

Table reports the calibration and validation results for the calibration catchments. Locations of in-situ stations are reported in Figure 3.5. Runoff coefficients are reasonable and consistent across the calibration catchments, with the exception of catchment 37, which shows an unreasonably high runoff coefficient when compared to the gauging data from station Khor. This could indicate problems with the IMERG precipitation estimates in this region or problems with the in-situ data (e.g. outdated rating curves). Performance during the calibration period is generally satisfactory for all catchments (average NSE is 0.59) and performance does not degrade significantly between calibration and validation periods, with the average NSE of all catchments remaining at 0.59, also for the validation period. This indicates that the model calibration is robust and model parameters are not over-fitted in the calibration. Climatology indices for the individual catchments are mostly positive for both the calibration and the validation period and, for some catchments, approach the value of 1. This indicates that the calibrated NAM rainfall-runoff models forced with IMERG precipitation perform significantly better than runoff prediction based on the long-term average observed runoff. The rainfall-runoff models were further validated at a number of downstream stations as reported in Table 4.1. These stations integrate runoff from a number of sub-catchments, including un-gauged sub-catchments that inherited rainfall-runoff model parameters from similar calibration catchments, and results indicate satisfactory performance in the downstream regions of both the Songhua tributary and the main Amur River. Overall, the evaluation of the rainfall-runoff models shows that the models predict runoff reliably; however, model errors due to the coarse spatial disaggregation, the uncertain climate forcings, and insufficient representation of human interventions (reservoir regulation, water abstractions) are significant, as is common for large-scale hydrological models of this type.

Table 4.1: Rainfall-runoff model validation at a number of in-situ discharge stations along the main Amur and Songhua rivers

Station	Validation Period	Average discharge (m^3/s)	RMSE (m^3/s)	RMSE (% of av. discharge)	WBE (m^3/s)	WBE (% of av. discharge)
Khaborovsk	2008-2018	8384	3305	39	1058	13
Komsomolsk	2012-2019	10259	3587	35	1227	12
Bogorodskoe	2008-2019	11459	3657	32	305	3
Harbin	2007-2014,2019	1156	633	55	-60	-5
Xiadaiji	2016-2020	922	476	52	200	22
Tonghe	2007-2014	1265	726	57	61	5
Yilan	2007-2014	1595	931	58	-212	-13
Jiamusi	2007-2014	1756	884	50	-30	-2
Mean				47		4

4.2. Results of river cross section delineation from ICESat-2

In total, 217 river cross sections were prepared from ICESat-2 datasets for the main Amur River and the Songhua tributary (Figure 4.1). The distance between cross sections varies, because the orientation of the river with respect to the ICESat-2 ground tracks is variable. In some south-north oriented river reaches, useable ground tracks are sparse and the cross sections are therefore less densely spaced. Figure 4.2 illustrates the cross section processing workflow and its results for one selected cross section on the Songhua River (Songhua chainage 960 km). Panel A of Figure 4.2 shows the ATL03 and ATL08 datasets along this ground track, passing over the river, which is braided in this location, and over the adjacent floodplains. Because the spatial resolution of ATL08 is relatively coarse, the product does not resolve important features such as dikes and levees, which control the hydraulic characteristics of the cross section. This is evident from Panel B in Figure 4.2, and clearly illustrates the added value of using the ATL03 product in the cross section retrieval workflow. Panel C shows the retrieved riverbed geometry after filtering and smoothing, including the submerged portion of the river, which is extrapolated using the power channel relationships. In this case, the cross section for the hydraulic model was limited to the region between the first major dikes on each side of the river and Mike Hydro River assumes vertical banks beyond the first and last points of the mapped cross section. This implies that the model would not correctly simulate extreme events in which the river overflows the dikes in this river reach. In this location, two major river channels are visible in the ICESat-2 dataset and extrapolation of the submerged portion was thus applied to both submerged sections of the transect, assuming equal water surface elevation and depth in both channels.

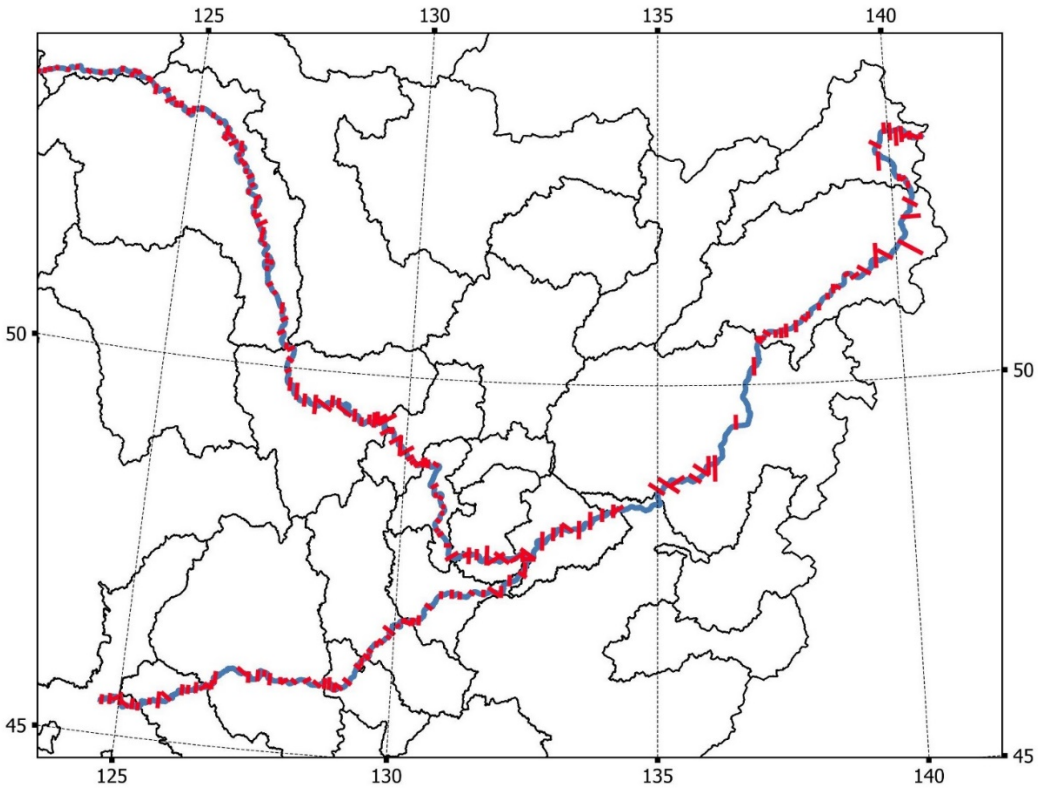

Figure 4.1: 217 river cross sections delineated from ICESat-2 datasets along the main Amur River and the Songhua tributary

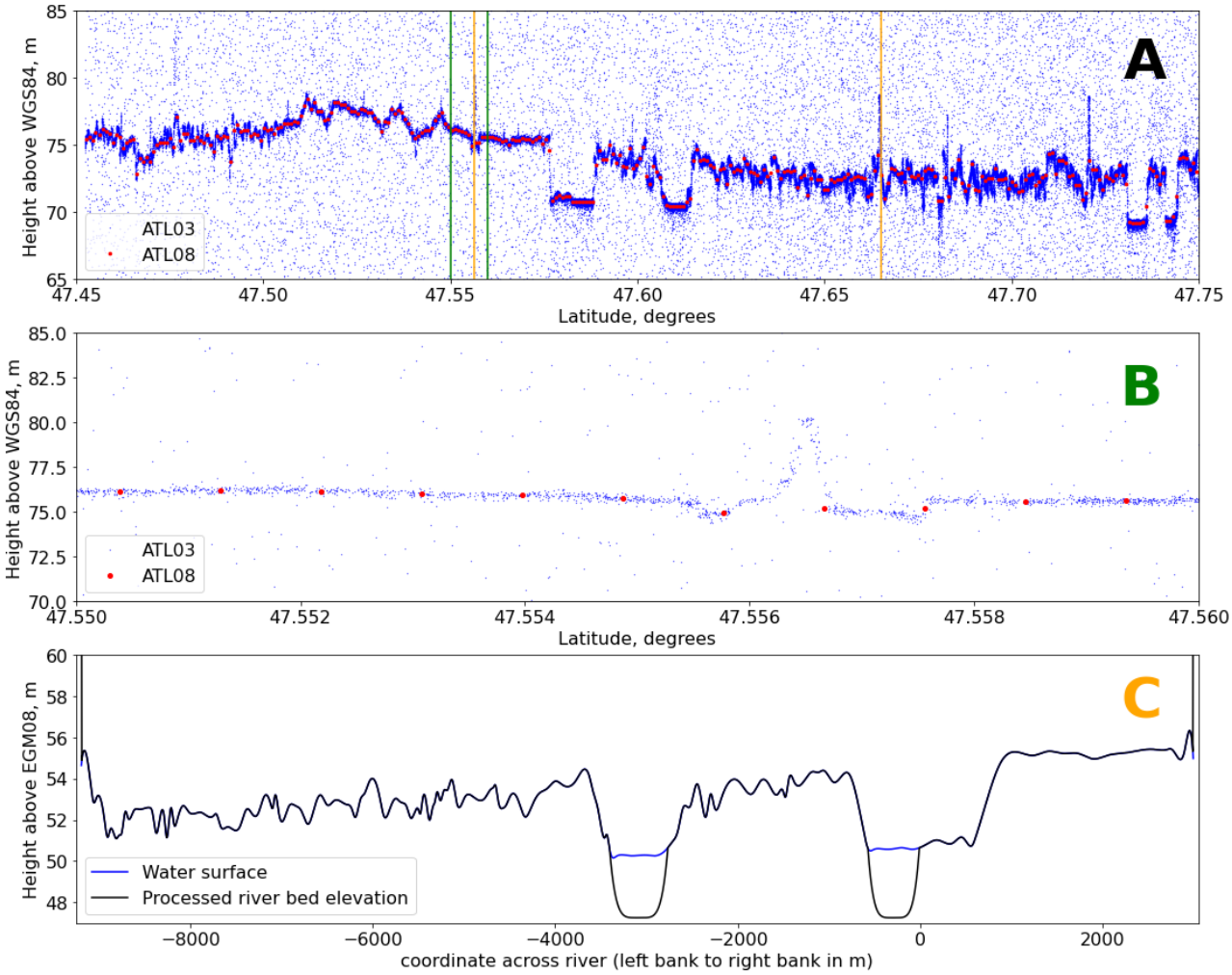

Figure 4.2: Illustration of the ICESat-2-based river cross section processing workflow and its results. Panel A: ATL03 and ATL08 cross section across the lower Songhua River (chainage 960 km). Panel B: Zoomed in view of panel A showing a levee running along the Songhua River, which is clearly mapped by ATL03 but not sampled in ATL08. Panel C: Processed cross section for inclusion into the hydrodynamic model. Please note reverse cross section orientation in C to comply with ascending coordinates left to right bank. ATL03 data is interpolated to 5m spatial resolution as described in section 3.3 of the report. The submerged portions of the cross section are extrapolated using the power channel relationships.

4.3. Hydraulic model results

Using the ICESat-2-derived river cross sections and the parameterization of Manning's roughness coefficient described in section 3, the hydraulic model was run for the period 2001-2021, using the runoff and tributary flow forcings provided by the rainfall-runoff models and the reservoir/river routing routine. Simulated WSE and discharge is thus available for a 20-year simulation period at any location of interest on the river network. Figure 4.3 compares selected examples of simulated WSE time series at in-situ and Hydroweb virtual stations with the corresponding in-situ and satellite radar altimetry observations. Generally, the fit to in-situ and satellite WSE is satisfactory with RMSE ranging from less than 1 to about 2.5 m, depending on station location (Figures 4.4-4.7, Table 4.3). The vast majority of Hydroweb and

Hydrocoastal L3 VS show RMSE values between 1 and 2 meters and bias values between -1 and +1 meter. The accuracy of the satellite altimetry observations is expected to be variable across the domain. For the wide rivers in the downstream portions of the basin, the accuracy of the altimetric WSE observations is probably around 0.5 m or better, while accuracy in the upstream, more narrow reaches is likely lower (Jiang et al., 2017, 2020). It is important to note that this performance was achieved without the use of any in-situ cross section geometry observations and without extensive calibration of the hydraulic model. Moreover, the error of the modelled WSE integrates errors in the rainfall-runoff/routing model, including reservoir regulation, and the hydraulic model. The only in-situ dataset used in model development is the in-situ gauging dataset used for calibration of the rainfall-runoff models. Spatial maps of RMSE and bias for the different VS clearly indicate spatial correlation of model errors (Figure 9), which could be mitigated by local adjustment of the Manning coefficient and flow depth. However, calibration of the hydraulic model is challenging, given the size of the model and the resulting computational load (ca 30 minutes of calculation time for a 20-year simulation period on a 3GHz Intel i5-9500 CPU with 16 GB RAM) and local refinement and calibration of the model should thus preferably be implemented using smaller-scale sub-models. Moreover, in view of potential global application of this modelling workflow, we would like to focus on a calibration-free cross section delineation workflow in this study and demonstrate that such a workflow can deliver WSE predictions with satisfactory accuracy.

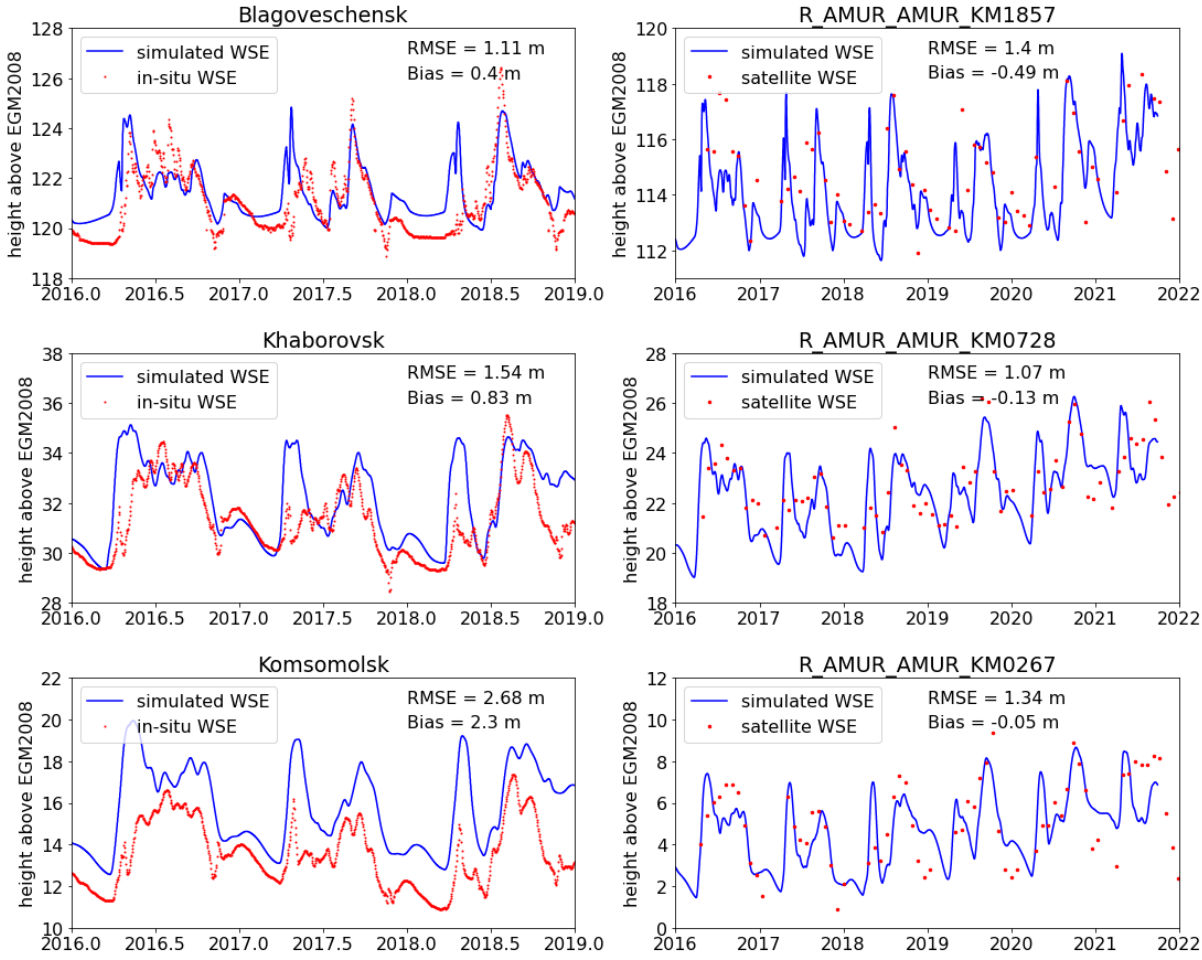

Figure 4.3: Comparison of simulated and observed WSE time series from selected in-situ stations (left) and virtual stations (right)

Table 4.2: Hydraulic model performance (after adjustment of depth) for in-situ stations along the Amur-Songhua

	RMSE of simulated WSE, m	Bias of simulated WSE, m
Nikolaevsk	0.44	0.08
Khaborovsk	1.54	0.83
Bogorodskoe	0.85	0.26
Komsomolsk	2.68	2.30
Innokentievka	1.45	0.87
Blagoveschensk	1.11	0.40
Jalinda	1.32	-0.54
Jiamusi	0.92	0.29
Yilan	0.85	0.08
Tonghe	1.49	-0.97
Harbin	0.92	0.13
Xiadaiji	2.47	2.16

Hydrocoastal L3 and Hydroweb VS datasets are about equally valuable for the validation of the hydraulic model derived from ICESat-2 elevation. As shown in Figures 4.4-4.7, VS density is somewhat higher in the Hydrocoastal L3 dataset than in the Hydroweb dataset. However, model bias and RMSE are slightly larger in the Hydrocoastal L3 dataset, which could indicate that marginal/low quality VS records are included in the Hydrocoastal L3 dataset, which have been removed from the Hydroweb dataset. Overall, we can therefore conclude that Hydroweb and Hydrocoastal L3 data are comparable for large-scale hydraulic modelling in the Amur River basin.

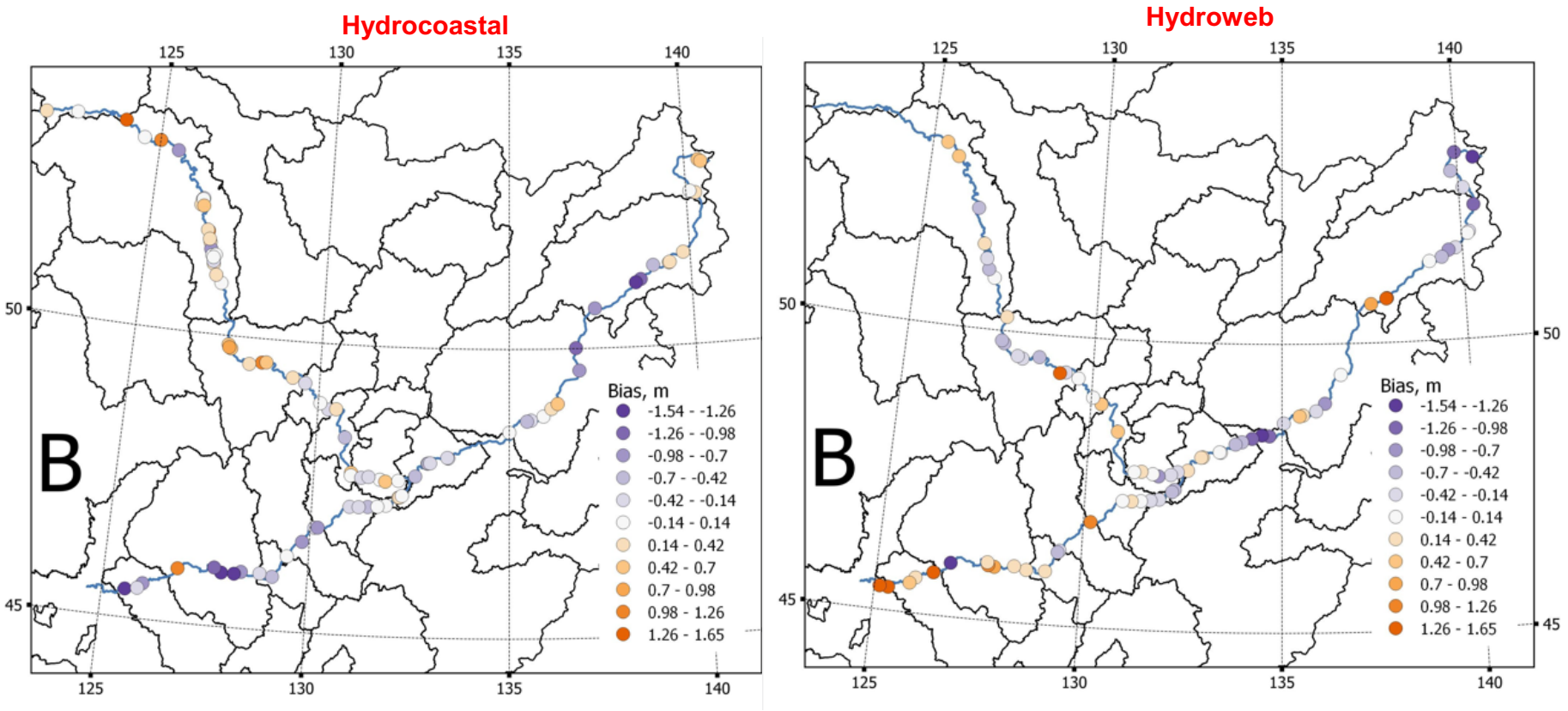

Figure 4.4: Overview of the spatial distribution of WSE bias at the different Hydroweb (right) and Hydrocoastal L3 (left) virtual stations.

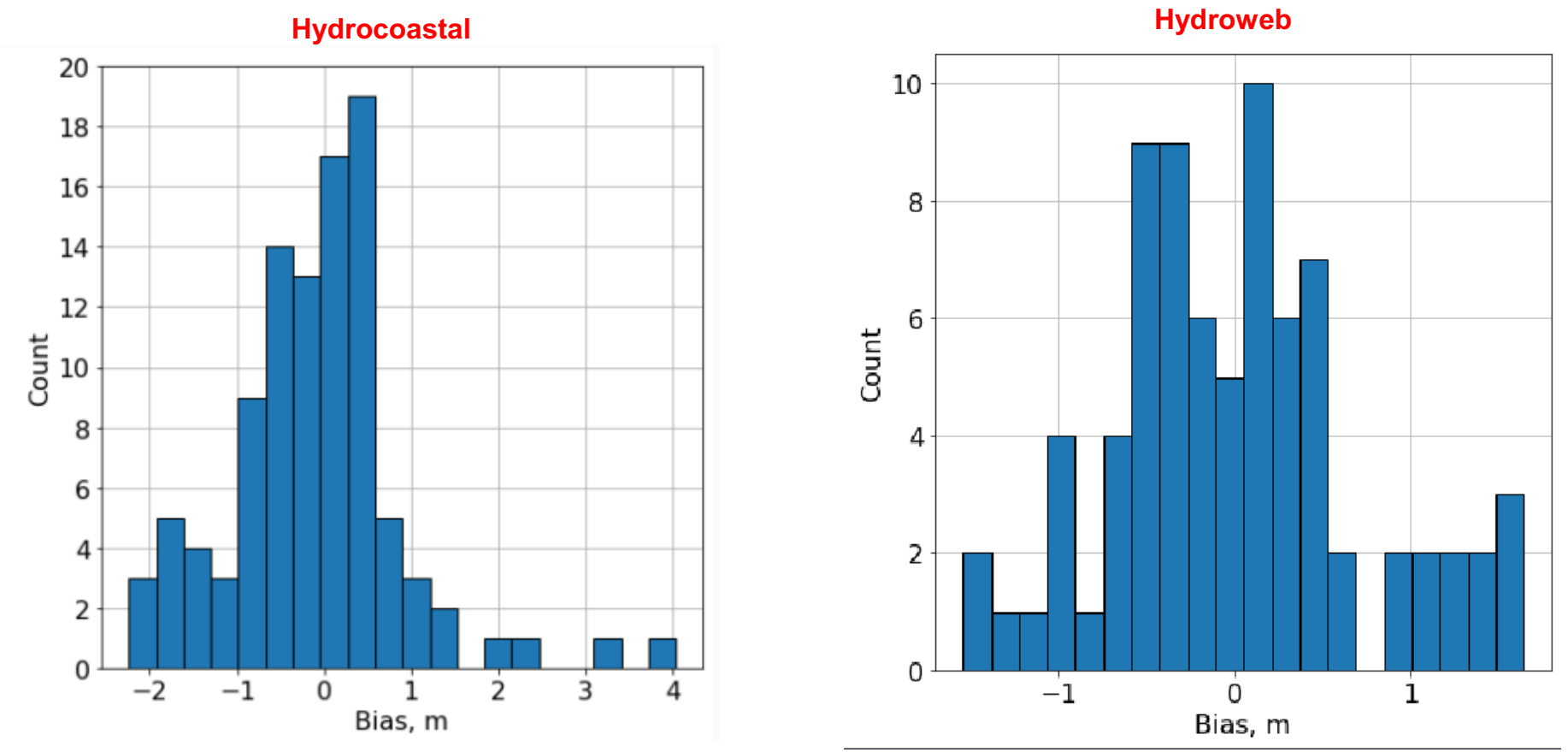

Figure 4.5: Histograms of water surface elevation bias for all Hydroweb (right) and Hydrocoastal L3 (left) virtual stations.

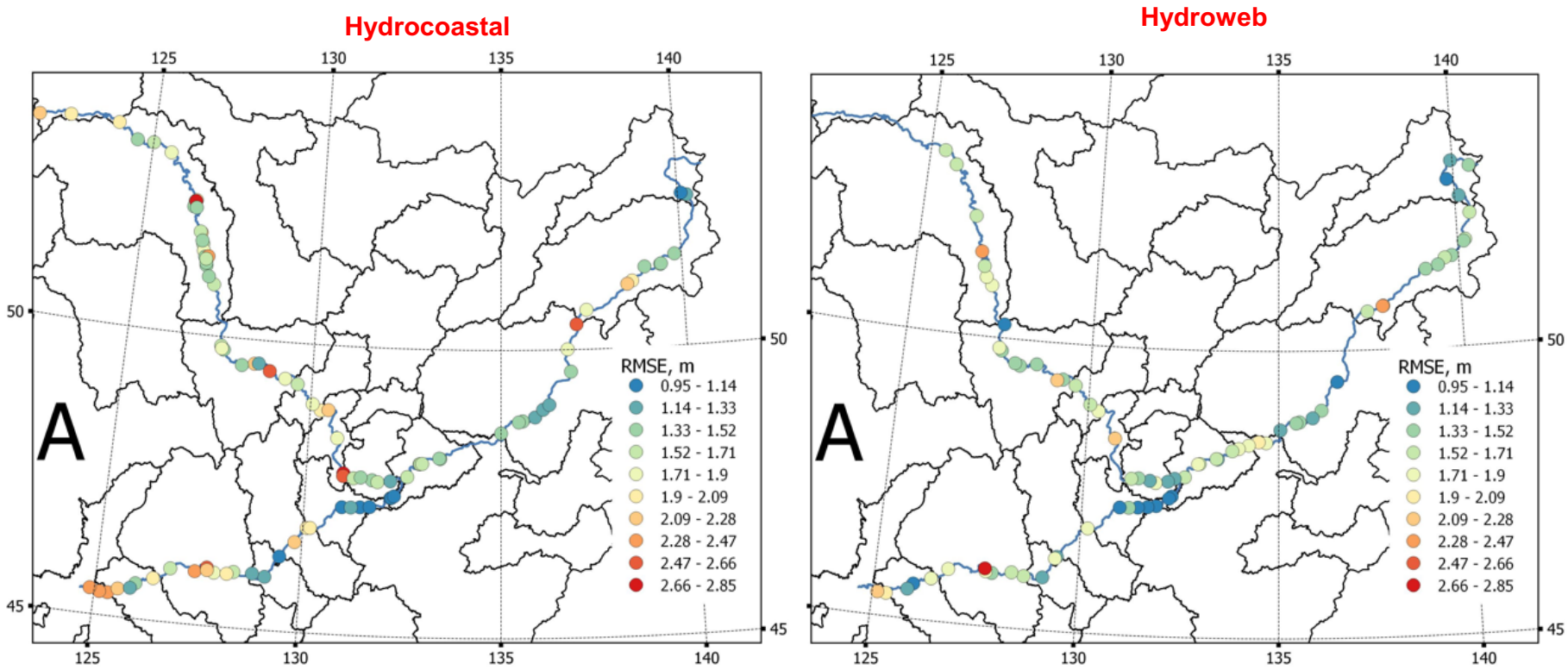

Figure 4.6: Overview of the spatial distribution of WSE RMSE at the different Hydroweb (right) and Hydrocoastal L3 (left) virtual stations.

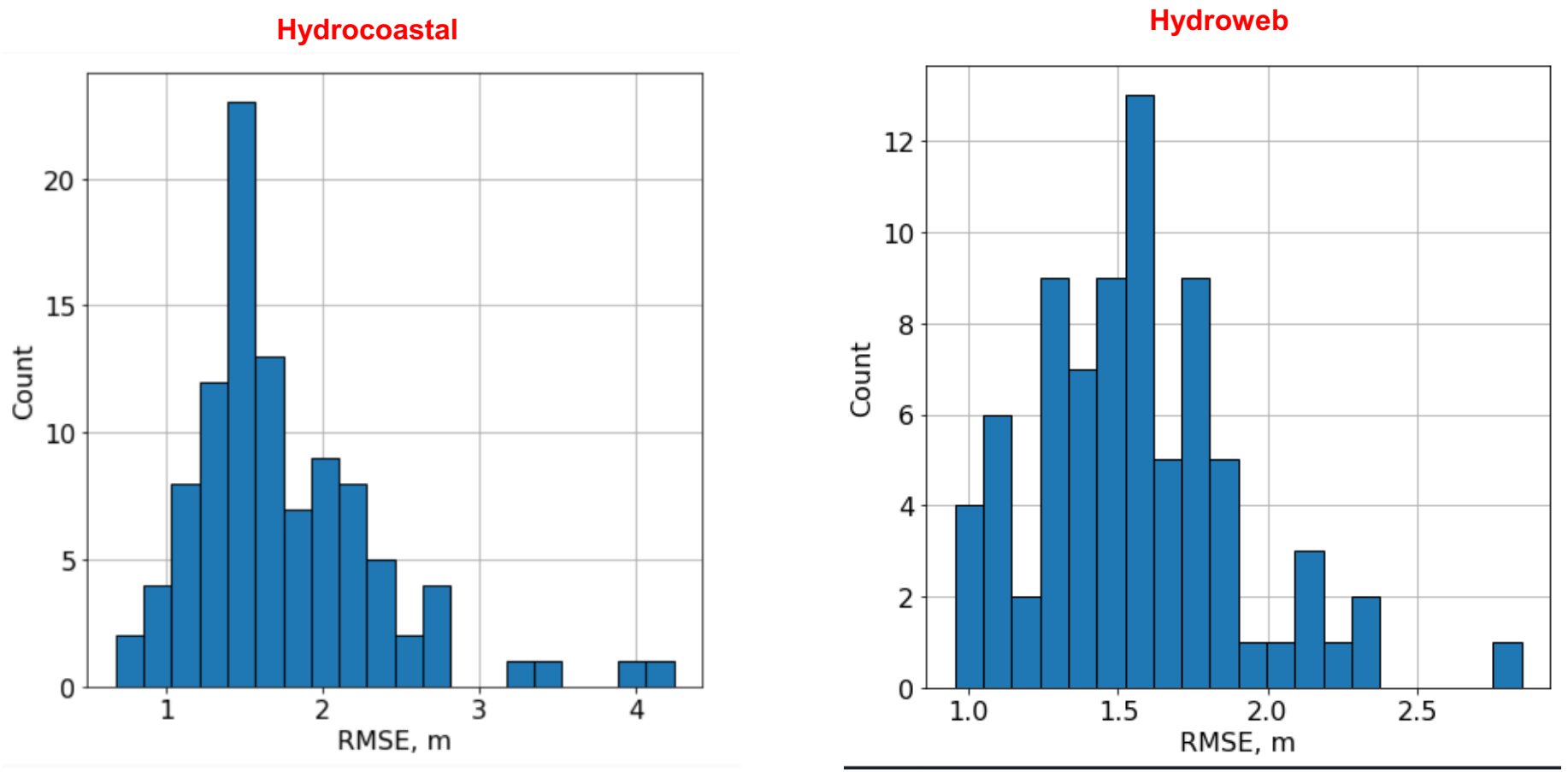

Figure 4.7: Histograms of water surface elevation RMSE for all Hydroweb (right) and Hydrocoastal L3 (left) virtual stations.

4.4. Model applications

Prospective model applications include the densification of satellite-derived WSE time series in space and time, the estimation of river discharge from satellite altimetry data, and the joint use of satellite EO data and the hydraulic model for operational hydraulic modelling and forecasting, using data assimilation (Schneider et al., 2018). Earlier studies have focused on the densification of WSE datasets from satellite altimetry using statistical interpolation techniques (Nielsen et al., 2022) or river width observations from satellite imagery (Tourian et al., 2016). Because such approaches do not require the development of a hydraulic model, they are efficient and suitable for global-scale application. However, the availability of ICESat-2 cross sections at global scale enables parameterization of global-scale hydraulic models from satellite remote sensing data only. Unlike statistical WSE densification workflows, densification using a hydraulic model respects the physical processes and phenomena occurring in the river and thus provides a physically consistent interpolation result.

The hydraulic model also provides rating relationships along the entire river course, as illustrated in Figure 4.8, including in-situ station locations and virtual station locations. Simulated rating relationships show two distinct branches, which correspond to the frozen and unfrozen periods with different Manning numbers. As shown in Figure 4.8 for the stations Khaborovsk and Komsomolsk, these two distinct branches of the rating relationship are also observable in the in-situ data. Because river gauging requires access to both banks of the river, no in-situ discharge data is available for the Amur River along a stretch of more than 1000 km, over which the river forms the border between Russia and China. Modelled rating relationships can be used to translate in-situ WSE records into estimated discharge in the transboundary river reach. The same can be done for any virtual station situated in the domain of the hydraulic model. Moreover, the hydraulic model can be used to investigate the shape and uniqueness of the rating relationship for different in-situ and virtual stations. For instance, the rating curve at Blagoveschensk is strongly affected by backwater effects originating from the confluence of the Amur and Zeya rivers (Liu et al., 2022), which is located a few kilometres downstream of the station. Such effects can also occur at virtual stations and the hydraulic model can be used to screen the available virtual stations for their suitability for discharge estimation using different types of rating relationships.

Finally, the basin-scale hydraulic model described here can provide boundary conditions for smaller-scale nested models of selected reaches and floodplains along the river. Local models can be refined using hydraulic inverse modelling techniques and can include interactions with the floodplains, using a coupled 1d-2d simulation approach. Prospectively, the workflow demonstrated here can be used to prepare a global-scale hydraulic model by combining riverbed geometry datasets from ICESat-2, global-scale rainfall-runoff simulation models and global-scale inland water elevation datasets from satellite altimetry, such as the Hydrocoastal and Hydroweb datasets.

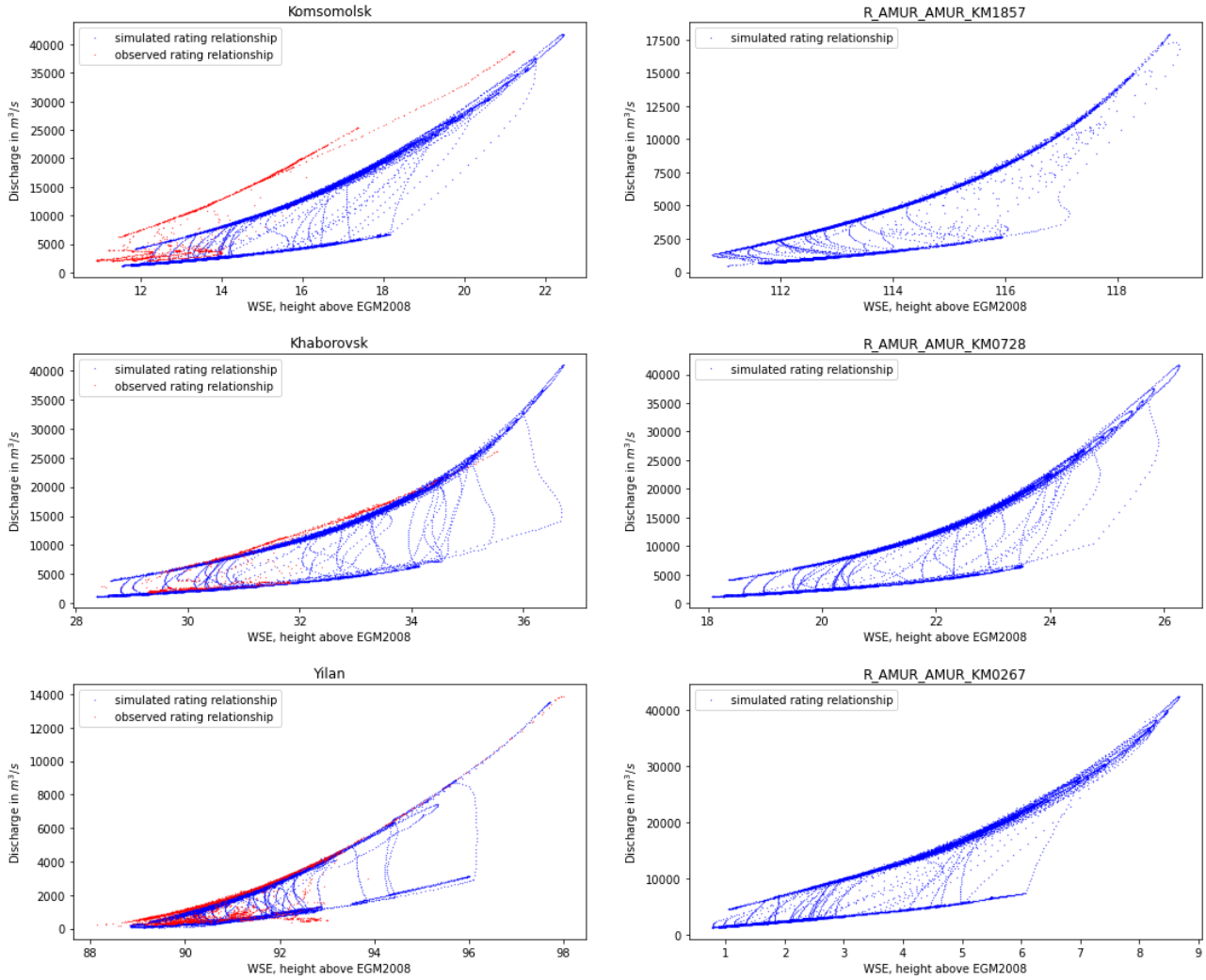

Figure 4.8: Simulated and observed rating relationships at selected in-situ stations (left) and virtual stations (right) on the Amur River

5. Conclusions

This report demonstrates a hydraulic modelling workflow for continental-scale rivers. Availability and quality of river cross-section geometry datasets is a common problem for hydraulic model development at this scale, especially in remote and poorly instrumented rivers, and this study demonstrates that ICESat-2 elevation datasets provide important new information in this context. ICESat-2 elevation datasets allow for the retrieval of reliable effective river cross section geometry and thus enable water surface elevation predictions along entire river courses at continental scale, which can be validated against the global spatio-temporally resolved water surface elevation record available from inland water satellite altimetry. The hydraulic modelling workflow developed here for the Amur is suitable for global-scale application and provides building blocks for operational, global-scale river water level prediction systems based on a combination of rainfall-runoff models, ICESat-2 elevation datasets, and satellite-based WSE observations.

The study used two different L3 river inland water level products, one provided by the Hydroweb platform and the new Hydrocoastal L3 inland water product, which was produced in the Hydrocoastal project. For the Amur River basin, and for the purposes investigated in this study, we see that both products perform approximately equally. The Hydrocoastal dataset provides time series at a somewhat higher number of virtual stations than Hydroweb (156 VS from Hydrocoastal vs 116 VS from Hydroweb). However, the quality of the VS time series in terms of accuracy and temporal coverage is somewhat lower for Hydrocoastal, which is most likely a consequence of the quality assurance and filtering procedures applied in the Hydroweb database. As also shown in the validation report of Hydrocoastal, the accuracy of L3 water level time series, evaluated by comparison with available in-situ water level records, did not significantly depend on the chosen retracking algorithm for the Amur VS. For the Hydrocoastal product to become a competitive alternative to Hydroweb and other existing databases, it is crucial to (1) ensure periodic near real-time updating of the VS time series, (2) build an easily accessible GIS-based user interface where users can download geographic and temporal subsets of the dataset in commonly used and easily understandable data formats, and (3) implement automatized quality assurance routines for VS time series to make sure that only time series with sufficient quality (i.e. sufficient accuracy and temporal coverage) are distributed to users.

6. Acknowledgements

This work has been partly funded by the European Space Agency Hydrocoastal project and supported by Innovation Fund Denmark through the ChinaWaterSense project (File number:8087-00002B) and the National Key Research and Development Program of China project (2018YFE0106500).

7. References

Abbott, M. B., & Ionescu, F. (1967). On the numerical computation of nearly horizontal flows. *Journal of Hydraulic Research*, *5*(2), 97–117. https://doi.org/10.1080/00221686709500195

Alfieri, L., Burek, P., Dutra, E., Krzeminski, B., Muraro, D., Thielen, J., & Pappenberger, F. (2013). GloFAS-global ensemble streamflow forecasting and flood early warning. *Hydrology and Earth System Sciences*, *17*(3), 1161–1175. https://doi.org/10.5194/hess-17-1161-2013

Alfieri, L., Pappenberger, F., Wetterhall, F., Haiden, T., Richardson, D., & Salamon, P. (2014). Evaluation of ensemble streamflow predictions in Europe. *Journal of Hydrology*, *517*, 913–922. https://doi.org/10.1016/j.jhydrol.2014.06.035

Andersen, H. E., Kronvang, B., Larsen, S. E., Hoffmann, C. C., Jensen, T. S., & Rasmussen, E. K. (2006). Climate-change impacts on hydrology and nutrients in a Danish lowland river basin. *Science of the Total Environment*, *365*(1–3), 223–237. https://doi.org/10.1016/j.scitotenv.2006.02.036

Andreadis, K. M., Schumann, G. J.-P., & Pavelsky, T. (2013). A simple global river bankfull width and depth database. *Water Resources Research*, *49*(10), 7164–7168. https://doi.org/10.1002/wrcr.20440

Arheimer, B., Pimentel, R., Isberg, K., Crochemore, L., Andersson, J. C. M., Hasan, A., & Pineda, L. (2020). Global catchment modelling using World-Wide HYPE (WWH), open data, and stepwise parameter estimation. *Hydrology and Earth System Sciences*, *24*(2), 535–559. https://doi.org/10.5194/hess-24-535-2020

Bennett, N. D., Croke, B. F. W., Guariso, G., Guillaume, J. H. A., Hamilton, S. H., Jakeman, A. J., Marsili-Libelli, S., Newham, L. T. H., Norton, J. P., Perrin, C., Fath, B. D., & Andreassian, V. (2013). Characterising performance of environmental models. *Environmental Modelling and Software*, *40*, 1–20. https://doi.org/10.1016/j.envsoft.2012.09.011

Bjerklie, D. M., Birkett, C. M., Jones, J. W., Carabajal, C., Rover, J. A., Fulton, J. W., & Garambois, P. A. (2018). Satellite remote sensing estimation of river discharge: Application to the Yukon River Alaska. *Journal of Hydrology*, *561*, 1000–1018. https://doi.org/10.1016/J.JHYDROL.2018.04.005

Chow, V. Te. (1988). *Applied hydrology* (D. R. Maidment & L. W. Mays, Eds.) [Book]. McGraw-Hill.

Crétaux, J.-F., Arsen, A., Calmant, S., Kouraev, A., Vuglinski, V., Bergé-Nguyen, M., Gennero, M.-C., Nino, F., Abarca Del Rio, R., Cazenave, A., Cazenave, A., & Maisongrande, P. (2011). SOLS: A lake database to monitor in the Near Real Time water level and storage variations from remote sensing data. *Advances in Space Research*, *47*(9), 1497–1507. https://doi.org/10.1016/j.asr.2011.01.004

Danilov-Danilyan, V. I., Gelfan, A. N., Motovilov, Y. G., & Kalugin, A. S. (2014). Disastrous flood of 2013 in the Amur basin: Genesis, recurrence assessment, simulation results. *Water Resources*, *41*(2), 115–125. https://doi.org/10.1134/S0097807814020055

Egidarev, E., Simonov, E., & Darman, Y. (2016). *Amur-Heilong River Basin: Overview of Wetland Resources BT - The Wetland Book: II: Distribution, Description and Conservation* (C. M. Finlayson, G. R. Milton, R. C. Prentice, & N. C. Davidson, Eds.; pp. 1–15). Springer Netherlands. https://doi.org/10.1007/978-94-007-6173-5_7-2

Garambois, P.-A., Calmant, S., Roux, H., Paris, A., Monnier, J., Finaud-Guyot, P., Samine Montazem, A., & Santos da Silva, J. (2017). Hydraulic visibility: Using satellite altimetry to parameterize a hydraulic model of an ungauged reach of a braided river. *Hydrological Processes*, *31*(4), 756–767. https://doi.org/https://doi.org/10.1002/hyp.11033

Hargreaves, G. H., & Samani, Z. A. (1985). Reference crop evapotranspiration from ambient air temperature. *Paper - American Society of Agricultural Engineers*.

Havnø, K., Madsen, M. N., & Dørge, J. (1995). MIKE 11 - A generalized river modelling package. *Computer Models of Watershed Hydrology*, 733 – 782.

Hock, R. (2003). Temperature index melt modelling in mountain areas. *Journal of Hydrology*, *282*(1–4), 104–115. https://doi.org/10.1016/S0022-1694(03)00257-9

Huffman, G. J., Stocker, E. F., Bolvin, D. T., Nelkin, E. J., & Tan, J. (2019). *GPM IMERG Final Precipitation L3 Half Hourly 0.1 degree x 0.1 degree V06*. https://doi.org/10.5067/GPM/IMERG/3B-HH/06

Jia, M., Mao, D., Wang, Z., Ren, C., Zhu, Q., Li, X., & Zhang, Y. (2020). Tracking long-term floodplain wetland changes: A case study in the China side of the Amur River Basin. *International Journal of Applied Earth Observation and Geoinformation*, *92*. https://doi.org/10.1016/j.jag.2020.102185

Jiang, L., & Bauer-Gottwein, P. (2019). How do GPM IMERG precipitation estimates perform as hydrological model forcing? Evaluation for 300 catchments across Mainland China. *Journal of Hydrology*, *572*, 486–500. https://doi.org/10.1016/j.jhydrol.2019.03.042

Jiang, L., Madsen, H., & Bauer-Gottwein, P. (2019). Simultaneous calibration of multiple hydrodynamic model parameters using satellite altimetry observations of water surface elevation in the Songhua River. *Remote Sensing of Environment*, *225*, 229–247. https://doi.org/10.1016/j.rse.2019.03.014

Jiang, L., Nielsen, K., Andersen, O. B., & Bauer-Gottwein, P. (2017). CryoSat-2 radar altimetry for monitoring freshwater resources of China. *Remote Sensing of Environment*, *200*. https://doi.org/10.1016/j.rse.2017.08.015

Jiang, L., Nielsen, K., Dinardo, S., Andersen, O. B., & Bauer-Gottwein, P. (2020). Evaluation of Sentinel-3 SRAL SAR altimetry over Chinese rivers. *Remote Sensing of Environment*, *237*. https://doi.org/10.1016/j.rse.2019.111546

Kalugin, A. S., & Motovilov, Y. G. (2018). Runoff Formation Model for the Amur River Basin. *Water Resources*, *45*(2), 149–159. https://doi.org/10.1134/S0097807818020082

Kittel, C. M. M., Arildsen, A. L., Dybkjær, S., Hansen, E. R., Linde, I., Slott, E., Tøttrup, C., & Bauer-Gottwein, P. (2020). Informing hydrological models of poorly gauged river catchments – A parameter regionalization and calibration approach. *Journal of Hydrology*, *587*. https://doi.org/10.1016/j.jhydrol.2020.124999

Kouraev, A. V., Zakharova, E. A., Samain, O., Mognard, N. M., & Cazenave, A. (2004). Ob' river discharge from TOPEX/Poseidon satellite altimetry (1992-2002). *Remote Sensing of Environment*, *93*(1–2), 238–245. https://doi.org/10.1016/j.rse.2004.07.007

Leopold, L. B., & Maddock Jr., T. (1953). The hydraulic geometry of stream channels and some physiographic implications. In *Professional Paper*. https://doi.org/10.3133/pp252

Liu, J., Jiang, L., Frias, M. C., & Bauer-Gottwein, P. (2022). Discharge estimates with stage-fall-discharge rating curves and ICESat-2 altimetry at backwater-affected virtual stations. *Earth and Space Science Open Archive*, 17. https://doi.org/10.1002/essoar.10512270.1

Maass, A., Hufschmidt, M. M., Dorfman, R., Harold A. Thomas, Jr., Marglin, S. A., & Fair, G. M. (1962). *Design of Water-Resource Systems - New Techniques for Relating Economic Objectives, Engineering Analysis, and Governmental Planning*. Harward University Press.

Madsen, H. (2000). Automatic calibration of a conceptual rainfall-runoff model using multiple objectives. *Journal of Hydrology*, *235*(3–4), 276–288. https://doi.org/10.1016/S0022-1694(00)00279-1

Markus, T., Neumann, T., Martino, A., Abdalati, W., Brunt, K., Csatho, B., Farrell, S., Fricker, H., Gardner, A., Harding, D., Yang, Y., & Zwally, J. (2017). The Ice, Cloud, and land Elevation Satellite-2 (ICESat-2): Science requirements, concept, and implementation. *Remote Sensing of Environment*, *190*, 260–273. https://doi.org/10.1016/j.rse.2016.12.029

Muñoz Sabater, J. (2019). *ERA5-Land hourly data from 1981 to present. Copernicus Climate Change Service (C3S) Climate Data Store (CDS)*. https://doi.org/10.24381/cds.e2161bace

Murray, A. M., Jørgensen, G. H., Godiksen, P. N., Anthonj, J., & Madsen, H. (2023). DHI-GHM: Real-time and forecasted hydrology for the entire planet. *Journal of Hydrology*, 129431. https://doi.org/https://doi.org/10.1016/j.jhydrol.2023.129431

Neal, J., Schumann, G., & Bates, P. (2012). A subgrid channel model for simulating river hydraulics and floodplain inundation over large and data sparse areas. *Water Resources Research*, *48*(11). https://doi.org/https://doi.org/10.1029/2012WR012514

Neuenschwander, A., & Pitts, K. (2019). The ATL08 land and vegetation product for the ICESat-2 Mission. *Remote Sensing of Environment*, *221*, 247–259. https://doi.org/10.1016/j.rse.2018.11.005

Neumann, T. A., Martino, A. J., Markus, T., Bae, S., Bock, M. R., Brenner, A. C., Brunt, K. M., Cavanaugh, J., Fernandes, S. T., Hancock, D. W., Skoog, J., & Thomas, T. C. (2019). The Ice, Cloud, and Land Elevation Satellite – 2 mission: A global geolocated photon product derived from the Aadvanced Ttopographic Llaser Aaltimeter Ssystem. *Remote Sensing of Environment*, *233*. https://doi.org/10.1016/j.rse.2019.111325

Nielsen, K., Zakharova, E., Tarpanelli, A., Andersen, O. B., & Benveniste, J. (2022). River levels from multi mission altimetry, a statistical approach. *Remote Sensing of Environment*, *270*. https://doi.org/10.1016/j.rse.2021.112876

Nielson, S. A., & Hansen, E. (1973). Numerical simulation of the rainfall-runoff process on a daily basis. *Nordic Hydrology*, *4*(3 (1973)), 171–190.

Nohara, D., Kitoh, A., Hosaka, M., & Oki, T. (2006). Impact of climate change on river discharge projected by multimodel ensemble. *Journal of Hydrometeorology*, *7*(5), 1076–1089. https://doi.org/10.1175/JHM531.1

Parrish, C. E., Magruder, L. A., Neuenschwander, A. L., Forfinski-Sarkozi, N., Alonzo, M., & Jasinski, M. (2019). Validation of ICESat-2 ATLAS bathymetry and analysis of ATLAS's bathymetric mapping performance. *Remote Sensing*, *11*(14). https://doi.org/10.3390/rs11141634

Pavlis, N. K., Holmes, S. A., Kenyon, S. C., & Factor, J. K. (2012). The development and evaluation of the Earth Gravitational Model 2008 (EGM2008). *Journal of Geophysical Research: Solid Earth*, *117*(4). https://doi.org/10.1029/2011JB008916

Pujol, L., Garambois, P. A., Finaud-Guyot, P., Monnier, J., Larnier, K., Mosé, R., Biancamaria, S., Yesou, H., Moreira, D., Paris, A., & Calmant, S. (2020). Estimation of multiple inflows and effective channel by assimilation of multi-satellite hydraulic signatures: The ungauged anabranching Negro river. *Journal of Hydrology*, *591*, 125331. https://doi.org/10.1016/J.JHYDROL.2020.125331

Savitzky, A., & Golay, M. J. E. (1964). Smoothing and Differentiation of Data by Simplified Least Squares Procedures. *Analytical Chemistry*, *36*(8), 1627–1639. https://doi.org/10.1021/ac60214a047

Schneider, R., Nygaard Godiksen, P., Villadsen, H., Madsen, H., & Bauer-Gottwein, P. (2017). Application of CryoSat-2 altimetry data for river analysis and modelling. *Hydrology and Earth System Sciences*, *21*(2), 751–764. https://doi.org/10.5194/hess-21-751-2017

Schneider, R., Ridler, M.-E., Godiksen, P. N., Madsen, H., & Bauer-Gottwein, P. (2018). A data assimilation system combining CryoSat-2 data and hydrodynamic river models. *Journal of Hydrology*, *557*, 197–210. https://doi.org/10.1016/j.jhydrol.2017.11.052

Schwatke, C., Dettmering, D., Bosch, W., & Seitz, F. (2015). DAHITI - An innovative approach for estimating water level time series over inland waters using multi-mission satellite altimetry. *Hydrology and Earth System Sciences*, *19*(10), 4345–4364. https://doi.org/10.5194/hess-19-4345-2015

Simonov, E. A., Nikitina, O. I., & Egidarev, E. G. (2019). Freshwater Ecosystems versus Hydropower Development: Environmental Assessments and Conservation Measures in the Transboundary Amur River Basin. In *Water* (Vol. 11, Issue 8). https://doi.org/10.3390/w11081570

Tachibana, Y., Oshima, K., & Ogi, M. (2008). Seasonal and interannual variations of Amur River discharge and their relationships to large-scale atmospheric patterns and moisture fluxes. *Journal of Geophysical Research Atmospheres*, *113*(16). https://doi.org/10.1029/2007JD009555

Tesfa, T. K., Tarboton, D. G., Watson, D. W., Schreuders, K. A. T., Baker, M. E., & Wallace, R. M. (2011). Extraction of hydrological proximity measures from DEMs using parallel processing. *Environmental Modelling & Software*, *26*(12), 1696–1709. https://doi.org/10.1016/J.ENVSOFT.2011.07.018

Tourian, M. J., Tarpanelli, A., Elmi, O., Qin, T., Brocca, L., Moramarco, T., & Sneeuw, N. (2016). Spatiotemporal densification of river water level time series by multimission satellite altimetry. *Water Resources Research*, *52*(2), 1140–1159. https://doi.org/10.1002/2015WR017654

Vansteenkiste, T., Tavakoli, M., Van Steenbergen, N., De Smedt, F., Batelaan, O., Pereira, F., & Willems, P. (2014). Intercomparison of five lumped and distributed models for catchment runoff and extreme flow simulation. *Journal of Hydrology*, *511*, 335–349. https://doi.org/10.1016/j.jhydrol.2014.01.050

Winsemius, H. C., Van Beek, L. P. H., Jongman, B., Ward, P. J., & Bouwman, A. (2013). A framework for global river flood risk assessments. *Hydrology and Earth System Sciences*, *17*(5), 1871–1892. https://doi.org/10.5194/hess-17-1871-2013

Yamazaki, D., Ikeshima, D., Sosa, J., Bates, P. D., Allen, G. H., & Pavelsky, T. M. (2019). MERIT Hydro: A High-Resolution Global Hydrography Map Based on Latest Topography Dataset. *Water Resources Research*, *55*(6), 5053–5073. https://doi.org/10.1029/2019WR024873

Yu, L.-L., Xia, Z.-Q., Li, J.-K., & Cai, T. (2013). Climate change characteristics of Amur River. *Water Science and Engineering*, *6*(2), 131–144. https://doi.org/10.3882/j.issn.1674-2370.2013.02.002

Zakharova, E., Agafonova, S., Duguay, C., Frolova, N., & Kouraev, A. (2021). River ice phenology and thickness from satellite altimetry: Potential for ice bridge road operation and climate studies. *Cryosphere*, *15*(12), 5387–5407. https://doi.org/10.5194/tc-15-5387-2021

Zhu, Y. P., Zhang, H. P., Chen, L., & Zhao, J. F. (2008). Influence of the South-North Water Diversion Project and the mitigation projects on the water quality of Han River. *Science of the Total Environment*, *406*(1–2), 57–68. https://doi.org/10.1016/j.scitotenv.2008.08.008